Ecological Applications, 28(5), 2018, pp. 1313–1324
© 2018 by the Ecological Society of America

Using imaging spectroscopy to detect variation in terrestrial ecosystem productivity across a water-stressed landscape

Sean DuBois,[1,2,3] Ankur R. Desai,[3,11] Aditya Singh,[2,4] Shawn P. Serbin,[5] Michael L. Goulden,[6] Dennis D. Baldocchi,[7] Siyan Ma,[7] Walter C. Oechel,[8,9] Sonia Wharton,[10] Eric L. Kruger,[2] and Philip A. Townsend[2]

[1]*ICF, Fairfax, Virginia 22031 USA*
[2]*Department of Forest and Wildlife Ecology, University of Wisconsin-Madison, Madison, Wisconsin 53706 USA*
[3]*Department of Atmospheric and Oceanic Sciences, University of Wisconsin-Madison, Madison, Wisconsin 53706 USA*
[4]*Department of Agricultural and Biological Engineering, University of Florida, Gainesville, Florida 32611 USA*
[5]*Environment and Climate Sciences Department, Brookhaven National Laboratory, Upton, New York 11973 USA*
[6]*Department of Earth System Science, University of California-Irvine, Irvine, California 92697 USA*
[7]*Department of Environmental Science, Policy, and Management, University of California-Berkeley, Berkeley, California 94720 USA*
[8]*Department of Biology, San Diego State University, San Diego, California 92182 USA*
[9]*Department of Geography, University of Exeter, Exeter EX4 4QD UK*
[10]*Atmospheric, Earth and Energy Division, Lawrence Livermore National Laboratory, Livermore, California 94550 USA*

Abstract. A central challenge to understanding how climate anomalies, such as drought and heatwaves, impact the terrestrial carbon cycle, is quantification and scaling of spatial and temporal variation in ecosystem gross primary productivity (GPP). Existing empirical and model-based satellite broadband spectra-based products have been shown to miss critical variation in GPP. Here, we evaluate the potential of high spectral resolution (10 nm) shortwave (400–2,500 nm) imagery to better detect spatial and temporal variations in GPP across a range of ecosystems, including forests, grassland-savannas, wetlands, and shrublands in a water-stressed region. Estimates of GPP from eddy covariance observations were compared against airborne hyperspectral imagery, collected across California during the 2013–2014 HyspIRI airborne preparatory campaign. Observations from 19 flux towers across 23 flight campaigns (102 total image-flux tower pairs) showed GPP to be strongly correlated to a suite of spectral wavelengths and band ratios associated with foliar physiology and chemistry. A partial least squares regression (PLSR) modeling approach was then used to predict GPP with higher validation accuracy (adjusted $R^2 = 0.71$) and low bias (0.04) compared to existing broadband approaches (e.g., adjusted $R^2 = 0.68$ and bias = −5.71 with the Sims et al. [2008] model). Significant wavelengths contributing to the PLSR include those previously shown to coincide with Rubisco (wavelengths 1,680, 1,740, and 2,290 nm) and V_{cmax} (wavelengths 1,680, 1,722, 1,732, 1,760, and 2,300 nm). These results provide strong evidence that advances in satellite spectral resolution offer significant promise for improved satellite-based monitoring of GPP variability across a diverse range of terrestrial ecosystems.

Key words: eddy covariance; gross primary productivity; hyperspectral imagery; HyspIRI; imaging spectroscopy; partial least squares regression.

Introduction

Recent work by Serbin et al. (2015) and Singh et al. (2015) has shown promising advancements in the use of hyperspectral imaging, collected from high-altitude airborne missions, to map the variation in the drivers of gross primary productivity (GPP) through measurement of leaf structure, metabolic capacities, and related biochemistry. While the use of broadband spectroscopy on tower, airborne, and satellite platforms to quantify seasonal variation in vegetation greenness, leaf area, and photosynthesis is well established (Carlson and Ripley 1997, Myneni et al. 2002, Heinsch et al. 2006), imaging spectroscopy affords new opportunities to more accurately monitor spatial and temporal variation in ecosystem function based on its sensitivity to leaf physiology. Imaging spectroscopy (also known as hyperspectral imagery) is here defined as reflectance data consisting of narrowband (5–10 nm) measurements across the full range of visible, near infrared and shortwave infrared wavelengths (VSWIR, 400–2,500 nm). Such high-dimensional data take advantage of narrow spectral features related to specific leaf functional, chemical, and structural traits (Curran 1989, Serbin et al. 2012).

In this study, we test an approach using imaging spectroscopy data collected across two years as part of the NASA HyspIRI Preparatory campaign to estimate GPP based on linkage to eddy covariance (EC) data from flux towers, which are currently the most widely used ground data for inferring ecosystem-level GPP. Although data from broadband sensors such as Landsat and MODIS have been used to generate GPP maps across large spatial scales (Running et al. 2004, Jung et al. 2011), the resulting estimates are subject to large biases and appear to primarily detect broad differences in GPP among ecosystem types and across vegetation density gradients, potentially missing physiological influences on GPP arising from variations in leaf traits responding to winter dormancy, plant stress, and stomatal response.

For example, the NASA Terra/Aqua-based MODIS GPP MOD17 product correlates well to flux tower GPP estimates, but, on average, monthly GPP overestimates site-level

Manuscript received 28 July 2017; revised 30 January 2018; accepted 14 March 2018; final version received 12 April 2018. Corresponding Editor: David S. Schimel.
[11] Corresponding Author. E-mail: desai@aos.wisc.edu

average GPP by 20%–30% across a range of land cover types compared to EC, with significant discrepancies between EC and MODIS emerging during phenological transitions (particularly spring green-up; Heinsch et al. 2006). As well, MODIS GPP did not capture spatial variability observed at the flux tower level between sites of similar vegetation type (Heinsch et al. 2006), especially at the regional scale. As such, a general conclusion is that MODIS may characterize broad variation among physiognomically different ecosystems by detecting differences in vegetation structure and/or cover rather than physiology.

The limits of current broadband remote-sensing techniques to accurately predict spatial or temporal GPP variation (Heinsch et al. 2006) provide an impetus to test the use of imaging spectroscopy to detect variation in vegetation function directly related to GPP. This is motivated by increasing evidence that hyperspectral data are sensitive to biochemical and physiological properties important to ecosystem function (Martin and Aber 1997, Smith et al. 2002, Ollinger and Smith 2005, Asner et al. 2007, Martin et al. 2008, Wolter et al. 2008, Ollinger 2011, Jetz et al. 2016, Lee et al. 2015, Schimel et al. 2015, Serbin et al. 2015, Singh et al. 2015). For example, high-resolution spectral data have the ability to capture variation in foliar concentrations of water, chlorophyll, cellulose, lignin, nitrogen, and other leaf constituents (Green et al. 1998), and studies have shown the ability to use hyperspectral data to map these and other leaf traits (Ustin and Gamon 2010, Serbin et al. 2012, Singh et al. 2015).

The NASA HyspIRI Preparatory Airborne mission provided an opportunity to collect a large quantity of high-resolution imagery across a range of EC flux towers in California covering numerous seasons across gradients of vegetation type, density, and physiology of temperate and semi-arid ecosystems with large variation in average GPP. Studied ecosystems ranged from coastal sage and valley grassland systems to high-elevation conifer forests. Our objective was to evaluate the ability of imaging spectroscopy data, through time and across multiple EC flux towers encompassing a range of ecosystem types, to estimate local-scale vegetation productivity. Flux tower measurements were combined with high-spectral and high-spatial resolution narrowband visible to shortwave infrared imaging spectroscopy, repeatedly captured at each tower site with high-altitude airborne sensors, to identify which spectral wavelengths, or combinations of multiple wavelengths (Inoue et al. 2008), relate most strongly to GPP variation within and across sites and compare the use of narrowband (400–2,500 nm) spectroscopy data for estimating GPP against existing approaches (e.g., from MODIS) that rely on broadband data.

Methods

Gross primary productivity estimates using eddy covariance

The EC flux towers span two climate/elevation gradients, a collection of wetland, grassland, and savanna sites in central California, and chaparral/coastal sage sites in southern California (Appendix S1: Table S1). The latitudinal and topographic gradients create a wide range of mean annual temperature and precipitation among the sites (Appendix S1: Fig. S1). Further, given the climatological wet season that typically lasts from late autumn to early spring, a number of ecosystem types and plant hydrological adaptations occur in this region, allowing us to observe a wide range of GPP patterns.

Three sets of sites were used here. One climate/elevation gradient crosses the San Jacinto Mountains in southern California, the other ascends from the San Joaquin Valley into the Sierra Nevada Mountains in central California, and the third set includes agricultural and wetland sites (Fig. 1). The southern California gradient includes the following sites (all site names corresponding with the dominant vegetation type): Grassland, Coastal Sage, and Oak–Pine Forest on the western slope of the San Jacinto Mountains, and Pinyon–Juniper Woodland, Desert Chaparral, and Sonoran Desert on the eastern slope (Kelly and Goulden 2008, Goulden et al. 2012), rising from 470 m elevation to 1,300 m and back down to 275 m in the desert (Table 1). The Sierra gradient is situated within the Upper Kings River watershed, and comprises grassland–savanna (Oak–Pine Woodland) and forest (Ponderosa Pine and Mixed Conifer) sites (Fig. 1), increasing in elevation from 405 to 2,015 m (Goulden et al. 2006).

The wetland and agricultural sites (pasture, rice paddy, and alfalfa) are near the San Joaquin River, in the grassland–savanna of the lower Sierra Nevada foothills, and grassland in the Altamont Hills. The wetlands (Twitchell East End Wetland and Mayberry Wetland) are recently restored (2010–2014) and the nearby agricultural fields (Twitchell Island, rice paddy; Twitchell Alfalfa, alfalfa field; Sherman Island, pasture) are actively managed. The sites located in the foothills are located on privately owned land and occasionally grazed by cattle. The Diablo grassland, located in the Altamont Hills, is owned by the Lawrence Livermore National Laboratory and is not actively managed. The southern California shrubland sites are located at the Sky Oaks Field Station (San Diego State University), with one flux tower in old-growth chaparral (Sky Oaks New) and the other in recently naturally burned (2003) chaparral (Sky Oaks Young).

From all 19 tower sites, half-hourly estimates of CO_2 flux were measured using the eddy covariance technique (Aubinet et al. 2011). We gap-filled missing and quality-screened data points using the Desai-Cook gap filling model (Cook et al. 2004, Desai et al. 2005). This model was applied to data filtered according to a turbulence threshold based on friction velocity (u^*), utilizing the 30-min averages for turbulent carbon flux or net ecosystem exchange (NEE). The model uses a variable moving-window mean diurnal variation method to estimate missing meteorological data, with the window size depending on the completeness of the data set. The Eyring function (Cook et al. 2004) was then applied to the data to estimate ecosystem respiration (R_{eco}). GPP was then estimated as the residual between the 30-min modeled R_{eco} and the measured NEE data. Variation in the estimated GPP was then related to 30-min averages for site photosynthetically active radiation (PAR) with a Michaelis-Menton reaction rate equation (Falge et al. 2001). The resulting models afforded GPP predictions when there were NEE gaps in the original data set, allowing us to adequately characterize seasonal and annual GPP dynamics (Baldocchi et al. 2015). However, comparisons to imagery were limited to periods when NEE observations were measured.

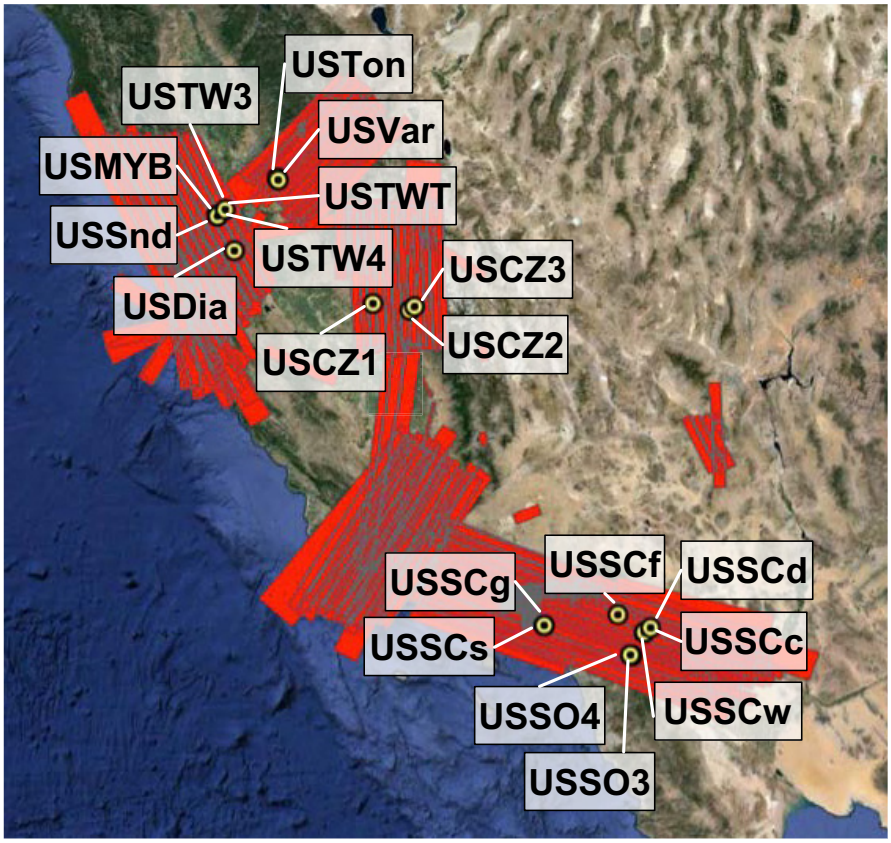

FIG. 1. Location of eddy covariance flux towers (circles) and all AVIRIS flight lines for the study region (California, USA) in 2013 and 2014 (imagery: Google Earth).

TABLE 1. Eddy covariance flux tower site information, including average temperature and precipitation anomalies for 2013–2014 against the average for 2003 through 2012.

Site name	Latitude (°N)	Longitude (°W)	SiteID	PFT classification	2013–2014 temperature anomaly (°C)	2013–2014 precipitation anomaly (percentage of average)
Twitchell Island	38.1055	121.652	USTWT	wetlands	1.5	61
Twitchell East End Wetland	38.103	121.641	USTW4	wetlands	1.8	61
Mayberry Wetland	38.0498	121.765	USMYB	wetlands	1.5	63
Tonzi Ranch	38.4316	120.966	USTon	grassland–savanna	1.3	58
Vaira Ranch	38.4067	120.951	USVar	grassland–savanna	1.3	58
Twitchell Alfalfa	38.1159	121.647	USTW3	grassland–savanna	1.5	61
Sherman Island	38.0373	121.754	USSnd	grassland–savanna	1.5	63
Diablo	37.6773	121.53	USDia	grassland–savanna	1.4	63
Oak–Pine Woodland	37.1087	119.731	USCZ1	grassland–savanna	1.5	32
Grassland	33.737	117.695	USSCg	grassland–savanna	1.6	36
Sierran Mixed Conifer Forest	37.0675	119.195	USCZ3	forest	1.3	34
Ponderosa Pine Forest	37.0310	119.257	USCZ2	forest	1.6	33
Oak–Pine Forest	33.808	116.772	USSCf	forest	1.8	51
Coastal Sage	33.734	117.696	USSCs	shrubland	1.6	36
Desert Chaparral	33.61	116.45	USSCc	shrubland	1.6	46
Pinyon–Juniper Woodland	33.605	116.455	USSCw	shrubland	1.6	46
Sky Oaks New	33.38443	116.64	USSO4	shrubland	1.5	58
Sky Oaks Young	33.3772	116.623	USSO3	shrubland	1.5	58
Sonoran Desert	33.652	116.372	USSCd	shrubland	1.5	43

Note: SiteID corresponds with Ameriflux Site ID (PRISM Climate Group, Oregon State University, http://prism.oregonstate.edu, created 17 May 2016).

Image acquisition

During the NASA HyspIRI Preparatory Campaign (Hochberg et al. 2015, Lee et al. 2015), all 19 flux tower sites were repeatedly overflown by the NASA ER-2 aircraft at 20 km, collecting imaging spectroscopy and thermal imagery using the AVIRIS (Airborne Visible/Infrared Imaging Spectrometer) and MASTER (MODIS/Advanced Spaceborne Thermal Emission and Reflection Radiometer Airborne Simulator) sensors (Fig. 1). The AVIRIS sensor measures reflected solar energy in the 380–2,510 nm spectral region with 224 spectral bands, with an average bandwidth of 10 nm (Vane et al. 1993, Green et al. 1998). Flights were conducted at several times throughout the dry and wet seasons and timed to capture maximum variation in plant phenology and ecosystem function (Appendix S1: Table S2).

The NASA Jet Propulsion Laboratory processed data, including radiometric calibration to surface reflectance following Thompson et al. (2015) and ortho-rectification and resampling to consistent 18-m pixels. To normalize between- and within-scene brightness offsets, we performed a brightness correction on all scenes following Feilhauer et al. (2010) as discussed in Serbin et al. (2015). Images were topographically corrected using the modified sun-canopy-sensor topographic method (Soenen et al. 2005), and cross-track changes in bidirectional reflectance distribution function (BRDF) were corrected using a quadratic function of the volumetric scattering term from the Ross-Thick BRDF model (Roujean et al. 1992, Lucht et al. 2000). Prior to analysis, we removed the five shortest and longest wavebands, along with those influenced by atmospheric water (1,313–1,453 nm and 1,782–2,018 nm), leaving 172 of the 224 channels of AVIRIS data over the 414–2,447 nm range.

Image data extraction from tower footprints

For each tower site, AVIRIS data were extracted only from cloud-free acquisitions. Locations of flux towers were identified within AVIRIS images using GPS coordinates, and spectra were extracted only from pixels containing within tower influence areas, as described below. The total number of acquisitions for our analysis was 102, encompassing 19 towers with an average of 5.4 acquisitions from multiple overflights during a 2-yr period (Table 1). To identify the vegetation influencing tower GPP, a one-dimensional online footprint model, based on Kljun et al. (2015), was used to estimate the size of the tower- influenced footprint at the time of each overflight. The model uses observations or estimates of conditions in the atmospheric boundary layer and canopy layer, including standard deviation of vertical velocity, surface friction velocity, instrument measurement height, boundary layer height, and roughness length. These were derived from the meteorological measurements made at the flux tower or, in the case of boundary layer height, assumed to be 1,500 m, for each overflight. Overlapping AVIRIS pixels were based on the upwind distance from the tower so as to encompass 90% of the total surface footprint influence. The footprint crosswind width was calculated as one-half the total length, so that the footprint was represented as a rectangle beginning from the base of the tower. The 18 × 18 m AVIRIS pixels from this footprint rectangle were then extracted for analysis, with the pixels in the footprint averaged to create a mean reflectance value for each AVIRIS band. The use of the footprint model allows us to address possible bias in flux tower measurements owing to different land cover or photosynthesis rates with direction and distance (Xu et al. 2017), a concern particularly at some of the more open and semi-arid sites.

Linking footprint imagery and tower flux data

We adopted two approaches to evaluate the sensitivity of imaging spectroscopy data to variation in GPP. First, we analyzed relationships between GPP and vegetation indices, which are routinely used in remote sensing of vegetation physiology (Roberts et al. 2011). We also statistically modeled GPP variation using partial least squares regression (PLSR) modeling approach, a chemometric method (Wold et al. 2001) that is often used for the analysis of hyperspectral imagery (Townsend et al. 2003, Martin et al. 2008, Wolter et al. 2008, Serbin et al. 2015, Singh et al. 2015) because it can exploit the full reflectance spectrum rather than select data subsets (such as vegetation indices) and doesn't assume the remote sensing data were measured without error. Furthermore, PLSR avoids collinearity in the predictor variables (i.e., wavelengths, indices) even when these exceed the number of observations (Geladi and Kowalski 1986, Wold et al. 2001, Carrascal et al. 2009). These issues are avoided by reducing the number of predictor variables down to relatively few, non-correlated, latent components, using a stepwise selection method with individual bands or indices (Grossman et al. 1996). These latent components capture other nuance in the relationship between the spectra and GPP (e.g., canopy structure, leaf physiology, nutrients; Asner and Martin 2008, Asner et al. 2011). PLSR is not a standard linear regression, and instead uses singular value decomposition (SVD) to reduce the predictor matrix to a much smaller set of predictor latent components, which are transformed through scores, weightings, and internal relationships to build the vector of regression coefficients by wavelength or index (Geladi and Kowalski 1986, Wold et al. 2001). This is not a limitation of PLSR but instead a feature of the approach that can allow for the dimensionality reduction of large problems to a much simpler model.

For the analysis of vegetation indices, we calculated Normalized Difference Spectral Indices (NDSI) for all combinations of the 172 wavebands in our VSWIR imagery, where, for each pair of bands (e.g., i and j), one band's reflectance value (Band_j) is subtracted from the other's (Band_i), and the difference is divided by their sum

$$\text{NDSI}[i,j] = [\text{Band}_i - \text{Band}_j]/[\text{Band}_i + \text{Band}_j]. \quad (1)$$

Normalized difference spectral indices offers the ability to examine all narrowband features, in this case 14,792 possibilities, and determine their relationship with ecosystem function, such as GPP (Inoue et al. 2008, Ryu et al. 2010). Normalization standardizes NDSI values from −1 to 1 and reduces atmospheric and BRDF effects not otherwise addressed in preprocessing. We note that the NDSI approach includes calculation of several widely used indices, including Normalized Difference Vegetation Index (NDVI,

normalized index of 850 and 650 nm; Tucker 1979) and Photochemical Reflectance Index (PRI, normalized index of 531 and 570 nm; Gamon et al. 1992). NDVI is of interest because of its wide use as a correlate with variation in aboveground vegetation structure and greenness, while PRI is related to stress-induced physiological responses (Penuelas et al. 1995, Gamon et al. 1997, Garbulsky et al. 2011). There are a vast number of additional multispectral and hyperspectral indices that have been correlated with vegetation function (Ustin et al. 2009), but the NDSI approach, covering all possible combinations of bands and their linear combinations, captures the variation expressed in those indices, so the only additional index we tested was a simple chlorophyll index (Gittelson and Merzlyak 1996), calculated as $[(1/R_{700}) - (1/R_{850}) - 0.1515]/0.01517$.

We first analyzed correlations between GPP and NDSI using data pooled across all sites, and then performed the same analysis on data subdivided by the four plant functional types (PFTs). Separating data into PFTs enabled assessment of the extent to which correlation was simply a consequence of broad differences in GPP across physiognomic vegetation types that look different in imagery (likely due to differences in physiognomy and/or soil fraction in the AVIRIS pixels), and subsequently whether image spectroscopy could detect variations within types independent of the structural differences among them.

PLSR, implemented in Python, was used to examine the relationship between flux tower and imagery data across the full reflectance spectrum, i.e., using all 172 wavebands. Typically, PLSR analyses are applied to reflectance from the 172 bands, enabling the exploitation of all information in the spectrum and resulting in an equation having a beta coefficient for reflectance in each waveband (Martin et al. 2008, Serbin et al. 2015, Singh et al. 2015). Here, we tested a new approach to PLSR, using the 14,792 NDSI combinations rather than reflectance bands as inputs. The closest 30-minute average GPP estimate to image acquisition was used to minimize the effects of diurnal changes in productivity. We performed 1,000 permutations of the data with a two-thirds–one-third split for calibration and validation. We determined the number of components to be used for model fitting by successively increasing the number of components from 1 to 15 until model validation statistics indicated overfitting. Once the number of components had been fixed, we extracted two-thirds of the data using a stratified random sampling strategy based on the land cover, and applied the model to the one-third of the withheld data for validation. In addition, to reflect uncertainties in the response variable, we added noise equivalent to 20% of each observation during each iteration by sampling from a normal distribution with a mean at the observation, and a standard deviation equal to 20% of the mean. This way, our modeling strategy accounts for uncertainties in data completeness by randomly dropping one-third of the tower sites, and in addition, accounts for uncertainties in the observations themselves. At each model iteration, we stored the PLSR coefficients, and present calibration and validation R^2, biases, and RMSEs as a percent of variation as model diagnostics. Table S4 (Appendix S1) shows overall model performance diagnostics, and diagnostics averaged across functional types. A heat graph of model coefficients by wavelength pairs was used to illustrate the importance of specific wavelengths and wavelength combinations as predictors of flux tower GPP from AVIRIS data. Use of NDSI rather than reflectance enables us to test whether identification of narrow absorption features is more predictive of vegetation function than magnitude of reflectance at a particular wavelength.

Last, we compared the predictive capacity of imaging spectroscopy from high-altitude AVIRIS against standard methods used to estimate GPP from broadband measurements. For this, we applied the broadband light-use efficiency method of Sims et al. (2008) to estimate satellite-derived GPP using Terra MODIS broadband-based enhanced vegetation index (EVI) and land surface temperature (LST), which has previously been shown to outperform the traditional and similar MOD17 GPP product by including a scalar to account for a water stress response of GPP (Sims et al. 2008). For the comparison, we convolved the AVIRIS wavelengths corresponding with the MODIS bands used to calculate EVI. We used LST estimates from the MODIS/ASTER airborne simulator (MASTER; Hook et al. 2001), which was acquired simultaneously with AVIRIS imagery (Lee et al. 2015). Sims et al. (2008) parameterized the scalar quantity m using three years of flux tower data. The model developed in Sims et al. (2008) requires mean annual nighttime LST estimates in the calibration of parameter m. However, there were not enough MASTER flights conducted at night to make this approach viable, so we instead used the mean of annual nighttime temperature calculated from flux tower data. Finally, we also compared the MODIS GPP product to tower GPP using the 1-km MODIS pixel encompassing the tower location (LP DAAC 2015). Tower GPP was then aggregated to 8-d estimates to match the MODIS product.

Results

The two-year study period occurred during a period of lower than average precipitation and higher than average temperature (Table 1; Appendix S1: Fig. S1). Over this time, among our 19 tower sites, the desert site recorded the lowest daily average tower-based GPP, 0.5 $\mu mol \cdot m^{-2} \cdot s^{-1}$, while the irrigated Twitchell Alfalfa site (USTW3), which becomes highly productive between cuttings, set the maximum, 25.6 $\mu mol \cdot m^{-2} \cdot s^{-1}$ (Fig. 2). The coefficient of variation for GPP (30-min average) at the time of AVIRIS overflights was 70% within individual tower sites, and 109% averaged across sites.

Heat graphs (Figs. 3 and 4) illustrate correlations between GPP (30-min average) at the time of overflight and NDSI calculated for each of the 14,792 waveband combinations in the corresponding footprint hyperspectral imagery. GPP and NDSI were closely correlated ($|r| > 0.6$) in broad regions of the spectrum when data were pooled across all sites (Fig. 3). In contrast, within vegetation types, strong correlations were generally restricted to narrower regions of the spectrum. Particular bands of high correlation include 414–434, 704–714, and 743–792 nm (Appendix S1: Table S3). In forests (Fig. 4a), high correlation ($|r| > 0.7$) occurred only when NDSI was generated from two groups of narrowband wavelength combinations, one based on 890–909 with 812 nm and another with 2,278–2,307 nm against 2,138–2,198 nm, reflective of larger differences in near

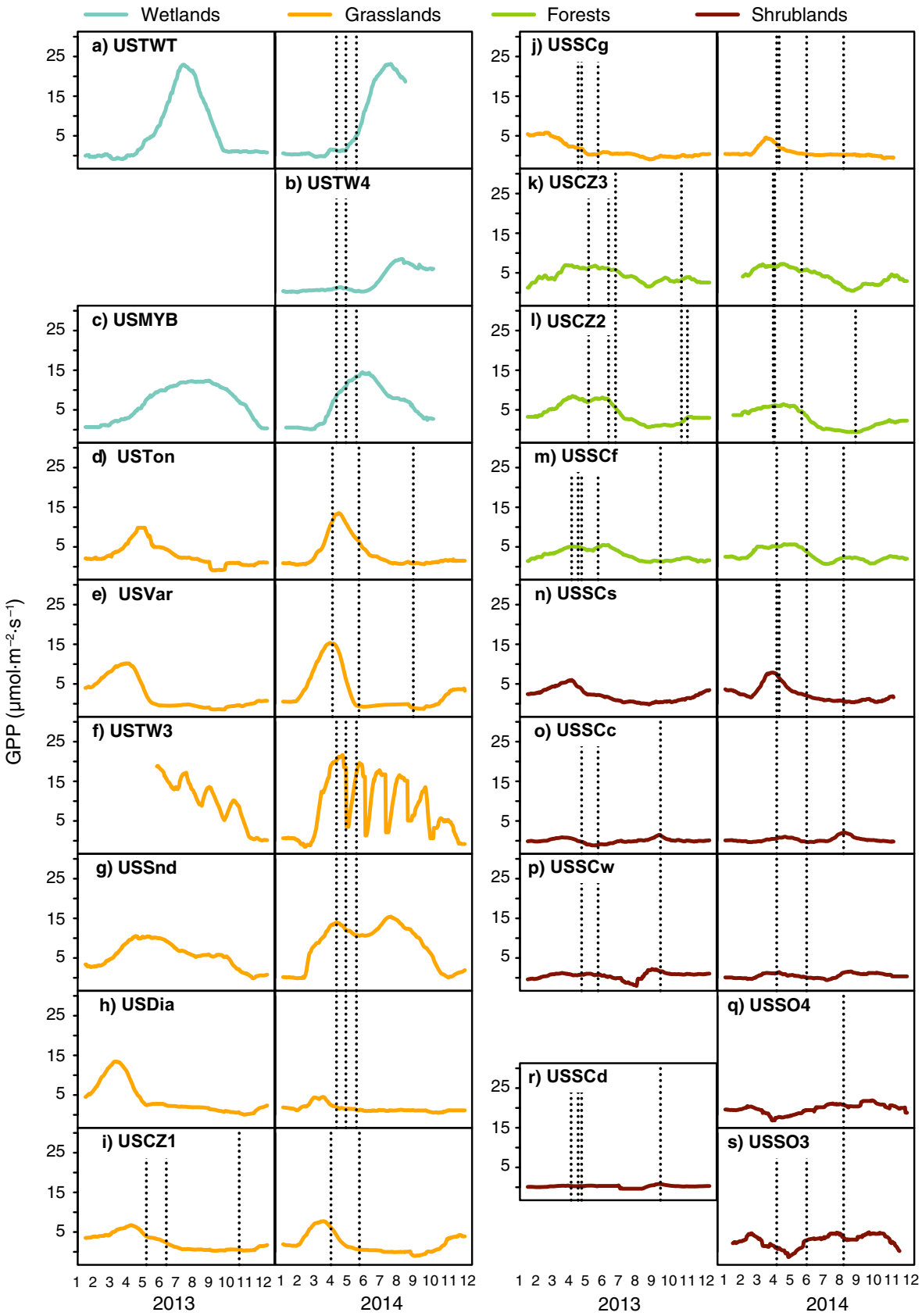

FIG. 2. Eddy covariance mean daily GPP for each study site, with flight imagery acquisition times noted by dotted lines. Colors represent site plant functional category used in analysis. Numbers on x-axis represent months, with 1 = January.

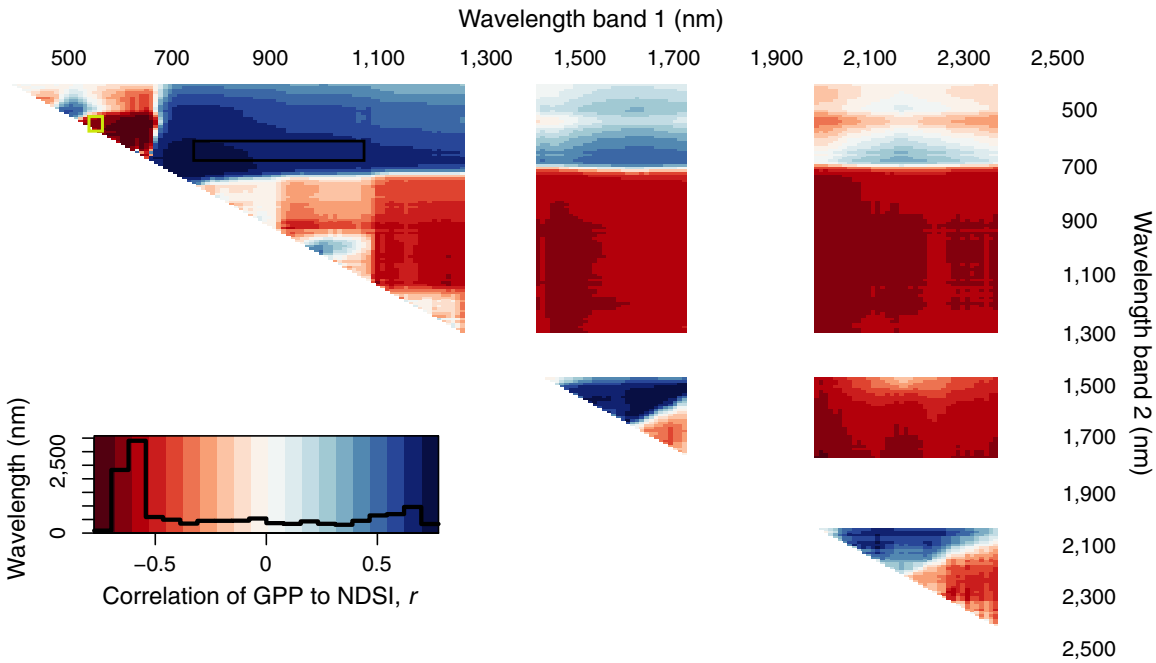

FIG. 3. Linear Pearson correlation coefficient of tower GPP to airborne imagery spectra normalized difference between all combinations of two bands (NDSI). Black box denotes general region and width of normalized difference vegetation index (NDVI) used by broadband sensors and yellow box the photochemical reflectance index. This figure includes all sites. Strong positive (blue) and negative (red) correlations exist in a number of broad spectral regions. Histogram depicts frequency of correlation on legend.

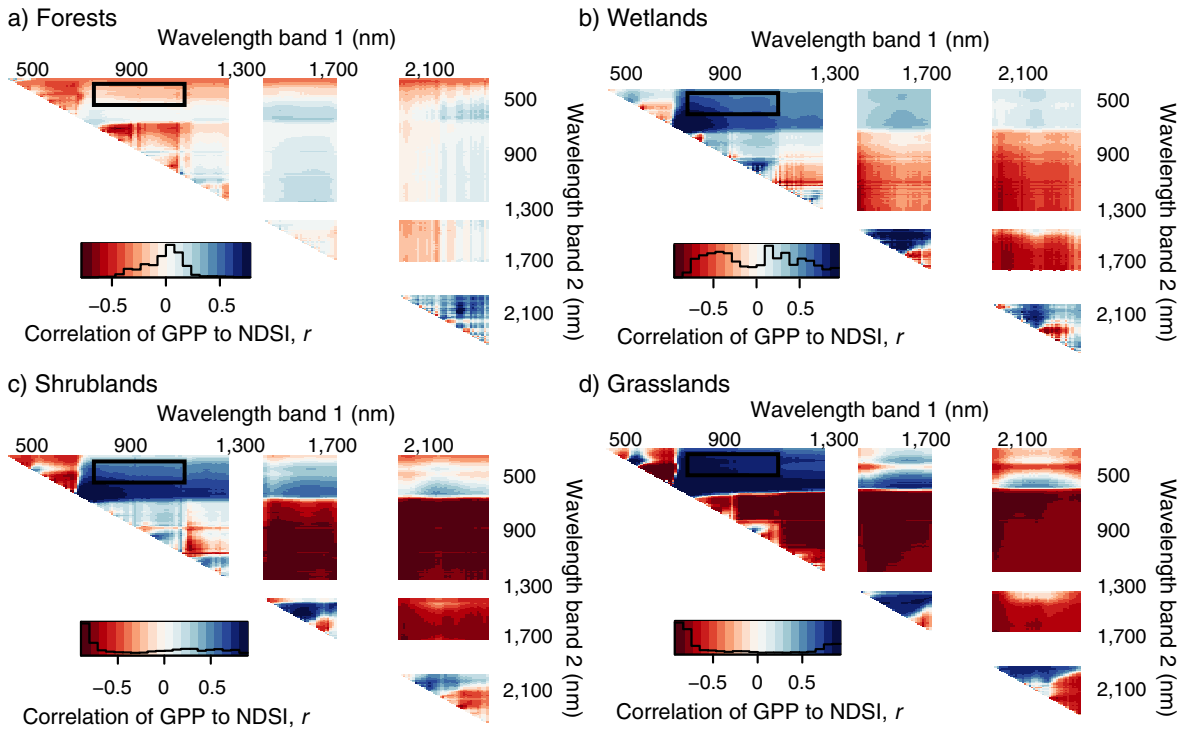

FIG. 4. Same as Fig. 3, but based on plant functional category, including (a) forests, (b) wetlands, (c) shrublands, and (d) grasslands. In contrast to Fig. 3, many areas of previously significant correlation disappear and those that persist are generally narrower in width. Red reflects negative correlation, blue for positive.

infrared albedo across forest types and changes in shortwave infrared related to canopy structure, water content, and leaf nitrogen. Among the widely used vegetation indices that we evaluated, NDVI and the chlorophyll index correlated with GPP (R^2 = 0.70 and 0.44, respectively) across all sites (Fig. 3), but these relationships were not significant within the forest type (Fig. 4, $P > 0.05$). PRI, on the other hand, did not correlate with GPP across sites ($P > 0.05$).

PLSR results reveal high fidelity in the ability to predict GPP across all sites and vegetation types ($R^2 = 0.78$, $P < 0.0001$, Fig. 5a), with all cover types performing similarly. The only significant difference between slopes of actual vs. predicted GPP occurred between grasslands and forest ($P = 0.0015$). Normalized PLSR coefficients (Fig. 6) indicate that an array of specific features, distributed throughout the entire spectrum, contribute substantively to the predictive model. Important narrow spectral regions in the predictive model included NDSI band combinations using 1,250–1,280 nm (combined in particular with wavelengths across the NIR), 2,030–2,050 nm, and 2,270–2,300 nm. Broader SWIR features important to the model incudes NDSIs in the 1,710–1,780 nm (when combined with 1,250–1,270 nm) and 1,500–1,680 nm regions (Fig. 6).

In contrast, the Sims broadband approach for remote estimation of GPP from spectra (Fig. 5b) is generally able to differentiate highest from lowest values of GPP across all types ($R^2 = 0.68$, $P < 0.0001$), but not as well as the PLSR approach, and does not accurately predict spatial and temporal variation in GPP within functional types. Slopes between actual and predicted GPP (Fig. 5b) vary significantly between grassland and forest ($P = 0.0044$), grasslands and shrublands ($P = 0.041$), and grasslands and wetlands ($P = 0.0041$). The models also deviate considerably from the 1:1 line compared the PLSR approach. This outcome is also replicated using other approaches such as the MODIS GPP product (MOD17A2.005; Appendix S1: Fig. S2).

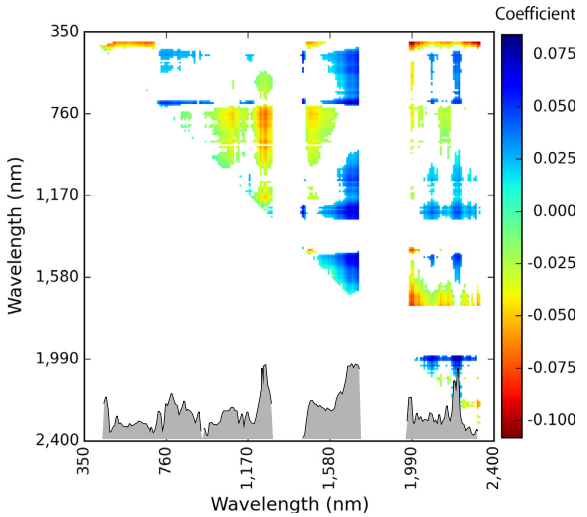

FIG. 6. Coefficients from the PLSR predicting EC-based GPP as a function of NDSIs based on all data pooled across all sites. Values plotted are mean coefficients, based on 1,000 permutations, and higher absolute values indicate higher contribution to the predictive model. Only NDSI combinations that were significantly different from zero across the 1,000 permutations are plotted. Also shown at bottom (shaded) is histogram of how frequently wavelengths appear in the PLSR predicting EC-based GPP as a function of NDSIs, based on all data pooled across all sites.

DISCUSSION

Water stress is likely one of the strongest drivers of large-scale GPP reductions globally (Ciais et al. 2005). Collectively, the results of this study illustrate the capacity of imaging spectroscopy to more accurately capture spatial and temporal variation in terrestrial ecosystem GPP over a water-stressed landscape, though additional years of observations over the same sites in non-drought conditions would be required to evaluate the full capability of the approach. In addition to its improved predictive capability relative to existing remote sensing approaches, an appealing advantage of the narrowband PLSR model we derived, relative to conventional broadband approaches, is that it does not require external inputs of meteorology or parameters related to plant ecophysiology.

Although the potential of imaging spectroscopy to track GPP has been shown at individual towers (Gamon 2015, Matthes et al. 2015) and with individual indices (Alton

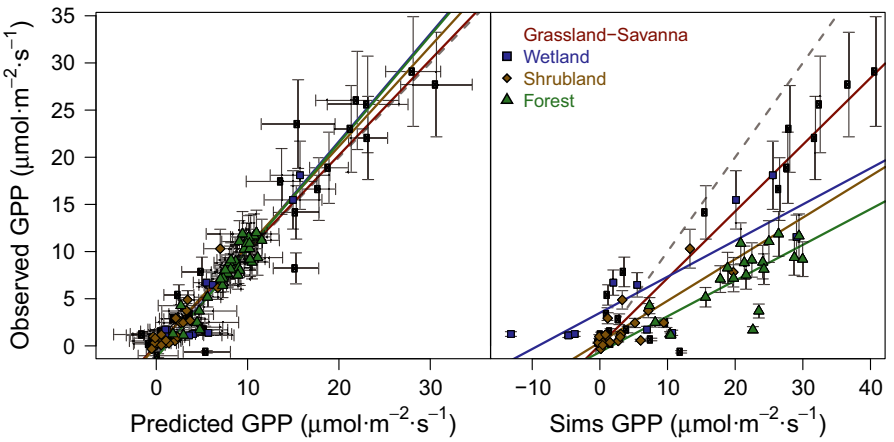

FIG. 5. Predicted 30-min average GPP (μmol·[m^{-2} ground area]·s^{-1}) derived by (a) partial least squares regression of NDSIs based on all airborne spectra and (b) airborne spectra simulated as broadband and applied to a widely used GPP model (Sims et al. 2008). While both models capture variability in flux tower GPP across all vegetation types, only the narrowband PLSR model (left) shows low bias (validation bias is 0.04 for the PLSR model and −5.71 for the Sims model) and similar performance for all cover types (Appendix S1: Table S4). Bars represent uncertainty in eddy covariance fluxes (vertical, calculated as 20% of the GPP value; Desai et al. 2008) and PLSR regression (horizontal, calculated as one standard deviation based off the 1,000 iterations of the PLSR model).

2017), our study is the first to demonstrate the capability across a diverse array of ecosystems, utilizing the full information content of narrowband spectra. Our results provide a robust initial assessment of the reliability of spatial extrapolation from hyperspectral imagery to justify the benefits of proposed future missions to GPP mapping (Schimel et al. 2015).

It is likely that a significant improvement in the fit over broadband occurs primarily from directly capturing the effects of physiology on GPP, which are highly variable over space and time. This improvement may be most noticeable in evergreen species, whose leaf phenology and density may be relatively constant, limiting broadband sensitivity to GPP variation. While a direct PLSR approach was not applied to the MODIS bands separately, the Sims model tested here represents the best-in-class for currently published MODIS based GPP algorithms. There are limitations in the comparison with the Sims model, as we were required to use air temperature rather than LST for the nighttime temperature measurements. However, modest adjustments in nighttime temperature parameters are unlikely to change the conclusion PLSR model outperformed the broadband-based model.

High correlations occurring with NDSIs at using wavelengths close to each other in the spectra indicate the importance of narrow features in the spectrum to vegetation properties that influence tower GPP. The heat graph of NDSI contributions to the PLSR model of GPP (Fig. 6) indicates several key narrowband combinations that are important to predicting tower GPP, especially in wavelength regions that have been shown to be important to vegetation physiology. Our findings mirror those of previous studies (Zarco-Tejada et al. 2001, Ryu et al. 2010, Matthes et al. 2015, Singh et al. 2015), which show a number of consistent regions of high correlation between GPP and narrowband NDSI. Ryu et al. (2010) used NDSI to compare spectra in the range of 400 and 900 nm with assimilation calculated using a similar flux partitioning method at the Vaira Ranch site between 2006 and 2009. The wavelength combinations associated with high and low correlation in the NDSI figure from the Ryu et al. (2010) study match the NDSI figure from this study for the grassland-savanna group of sites, which includes the Vaira Ranch site. The broad areas of high correlation for the given spectral range are present in both figures, as are the narrow features of low correlation associated with indices involving 700 nm and the range 400–700 nm, and 750 nm and the range 750–900 nm. Unlike Ryu et al. (2010), we were also able to demonstrate consistently important wavelengths in the shortwave infrared (SWIR, >1,100 nm).

Our findings confirm that specific features are associated with leaf/canopy spectral traits that reflect variation in leaf structure and function. The wavelengths significant to our PLSR model coincide with important physiological features, which is consistent with previous analyses showing AVIRIS wavelengths can be used to predict photosynthetic capacity via known features as opposed to simply measuring canopy structure (Serbin et al. 2015). Narrow NDSI combinations of wavelengths in the SWIR (2,050 nm) and near infrared (760 nm) appear especially influential, as do some broader features around 1,200, 1,600 and 2,200 nm. For the shortwave infrared regions, RuBisCo has known spectral absorption features around wavelengths 1,500, 1,680, 1,740, 2,050, and 2,290 (also: 1,940, 2,170 and 2,470 nm; Elvidge 1990), while significant wavelengths in the leaf-level V_{cmax} model presented in Serbin et al. (2012) occur at 1,510, 1,680 and 1,760, nm (also 1,940, 2,210, and 2,490 nm). Using AVIRIS imagery, Serbin et al. (2015) identified key features at 1,158–1,168, 1,722–1,732 and 2,300–2,400 nm.

In contrast, across all sites, the visible and near infrared regions (VNIR, 400–1,100 nm) did not exhibit as many key features for predicting GPP as did the SWIR. However, key narrow features do appear in the chlorophyll *a* absorption wavelengths at 414–434 nm, the red-edge (704–714 nm), and in the NIR (743–792 nm, including 763 nm, near a well-documented chlorophyll fluorescence feature). Spectral features such as the broader red edge (690–750 nm) are unsurprising as they are known to shift under water stress conditions (Vogelmann et al. 1993), one of the major contributors to variations in GPP in the ecosystems of California that were strongly affected by drought during our study period (Asner et al. 2016). These findings demonstrate that the improved predictive performance of a model based on imaging spectroscopy likely results from exploiting multiple mechanistic links among observed plant pigments, traits, and functional response.

Using the NDSIs (rather than raw reflectance wavelengths) allows the identification of combinations of narrow features (one or two wavebands wide) that appear repeatedly as important in our model. The heat graph for the PLSR coefficients using NDSI show a range of narrow features with high contribution to the PLSR (e.g., 2,288 nm) and wider features indicating broader correlations, likely related to vegetation water content (e.g., 1,503–1,682 nm). In particular, combinations of narrow wavebands centered on 414, 1,762, 2,048 and 2,298 appeared repeatedly in the PLSR model (indicated by streaks in the heat graph in Fig. 6). The value to PLSR used in the way presented here is that we were able to exploit both the full spectrum in the PLSR, but also narrow features at specific wavebands that emerged in the important NDSIs in the model.

The differences between the correlation heat maps (Figs. 3 and 4) and PLSR heatmap (Fig. 6) demonstrate the value of the imaging spectroscopy and PLSR approaches in estimating GPP across broadly varying ecosystems. Simple correlations with NDSI in which all cover types are pooled (Fig. 3) indicate that broad areas of the spectrum characterized by widely used indices such as NDVI, rather than narrow features that require imaging spectroscopy, are sufficient to capture major variation in GPP that is largely attributable to differences in physiognomic cover type (e.g., forest vs. grassland–savanna). This suggests decent discrimination of differences between types but poor predictability within types (Fig. 5b).

In contrast, the correlation heat graph broken out by cover type (Fig. 4) shows widely differing correlations between GPP and hyperspectral NDSIs by type, and indicates that both narrow and broad regions within different cover types are important correlates with GPP. Moving to a predictive framework, the PLSR of all data using NDSIs (Figs. 5a and 6) demonstrates that the imaging spectroscopy data, using NDSIs, can effectively discriminate variations in GPP encompassing differences between and within cover types.

When contrasted with broadband approaches (Fig. 5a vs. 5b), both imaging spectroscopy and broadband analyses adequately capture variations associated with type differences, although the imaging spectroscopy model exhibits less bias (Fig. 5a) than the broadband model (Fig. 5b), with the imaging spectroscopy PLSR approach standing out in that the different cover types more closely align along the same 1:1 line than the broadband approach. The limited data set does not allow in depth analysis of model performance for each vegetation type, but the model generated more accurate predicted GPP for grassland–savanna, shrubland, and wetland sites, while the forest type exhibited the lowest correlation (Appendix S1: Table S4). The NDSI values associated with the forest set of sites also exhibited the lowest overall average correlation (Fig. 4). The lower relative performance of both the model and average NDSI correlation for forest sites compared to the other types is expected, as the LAI for these sites is relatively constant throughout the growing season, as compared to other sites with a less dense canopy. Broad spectral areas of correlation (Fig. 4) are prevalent in sites where LAI is highly correlated with ecosystem productivity. For this reason, broadband-based productivity models can generally perform well across vegetative types, while the relationship breaks down within a classification (Fig. 5b). Furthermore, variation within a single site has been difficult to detect with all existing models examined, but the narrow-band-based model presented in this study is able to maintain low error and bias within vegetation types, including forest sites, which produced the lowest adjusted R^2 value (0.32). The result of this ability to capture variability within PFTs is a more robust model when compared to broadband based predictive models including the Sims model (Fig. 5). We provide the first evidence that a complex range of sites can be well simulated with no additional information beyond the spectral content and the PLSR model. Additional research and sampling is required to examine potential methods to improve predictability within forest sites.

Collectively, these analyses enable us to determine the capacity to extrapolate ecosystem function derived from flux tower data using hyperspectral imagery, and then infer ecosystem responses to climate anomalies such as the unprecedented drought that occurred in California during our study period (Asner et al. 2016). Challenges remain in handling diverse canopy architecture, especially open canopies with large soil exposed gaps, and integrating across complex terrain, land management, and seasonally stressed ecosystems (Kobayashi et al. 2012). Additional measurements across a wider range of climatic and ecological conditions will be required to develop a useful model at broader scales. Nonetheless, our findings have an important bearing on proposed future satellite-borne imaging spectroscopy missions that could fill the gaps in the globally sparse network of EC flux towers (Schimel et al. 2015).

Conclusion

Flux tower estimates of GPP across multiple ecosystems in a water-stressed region offer important observations that can inform remote sensing algorithm development for improved detection of drought impacts on carbon cycling and plant productivity. PLSR models based on imaging spectroscopy with high spectral resolution are capable of accurately predicting GPP independent of vegetation type and season, with significant improvement over traditional broadband approaches. Use of NDSIs in our PLSR models enabled us to leverage not only the full spectrum, as is common with hyperspectral imagery, but also narrow features identifiable in combinations of narrow bands, which has not typically been done in hyperspectral analyses, as usually just reflectance by wavelength is used.

Our findings provide the opportunity to accurately map ecosystem properties where broadband sensor capabilities are limited and suggest that spectral resolution is as or even more important than spatial resolution in consideration of future sensor design for satellite remote sensing. Further, there is strong evidence for mechanistic links among wavelengths and response associated with specific elements in leaf structure that influence plant productivity, and therefore GPP, on a canopy scale. We conclude that the sensitivity of ecosystem metabolism to ongoing and future climatic changes can be monitored continuously at high spatial resolution using satellites equipped with sensors similar to the proposed HyspIRI imaging spectrometer.

Acknowledgments

S. DuBois, A. R. Desai, A. Singh, S. Serbin, E. Kruger, and P. Townsend acknowledge support for this project by a NASA HyspIRI Preparatory Project award #NNX12AQ28G made to U. Wisconsin. Support for eddy covariance flux tower measurements and databases comes from the Department of Energy Office of Science Ameriflux Network Management Project. S. Serbin was supported by the United States Department of Energy contract No. DE-SC0012704 to Brookhaven National Laboratory in the writing of this manuscript. Flux tower data are available from the DOE Ameriflux database (http://ameriflux.lbl.gov/) or by direct contact to the PI. HyspIRI airborne imagery is available from the NASA AVIRIS data portal (https://avirisng.jpl.nasa.gov/alt_locator/). PLSR model code and results are available online at Figshare (https://doi.org/10.6084/m9.figshare.6020153). Spectroscopy data used in this study are available at the EcoSIS repository (https://ecosis.org/#result/fac4e3cb-7ebb-42d9-a7e3-1273114d4efa). The authors thank Andrew Jablonski for assistance with image processing.

Literature Cited

Alton, P. B. 2017. Retrieval of seasonal Rubisco-limited photosynthetic capacity at global FLUXNET sites from hyperspectral satellite remote sensing: impact on carbon modeling. Agricultural and Forest Meteorology 232:74–88.

Asner, G. P., and R. E. Martin. 2008. Spectral and chemical analysis of tropical forests: scaling from leaf to canopy levels. Remote Sensing of Environment 112:3958–3970.

Asner, G. P., D. E. Knapp, T. Kennedy-Bowdin, M. O. Jones, R. E. Martin, J. W. Boardman, and C. B. Field. 2007. Carnegie Airborne Observatory: in-flight fusion of hyperspectral imaging and waveform light detection and ranging for three-dimensional studies of ecosystems. Journal of Applied Remote Sensing 1:013536.

Asner, G. P., R. E. Martin, D. E. Knapp, R. Tupayachi, C. Anderson, L. Carranza, P. Martinez, M. Houcheime, F. Sinca, and P. Weiss. 2011. Spectroscopy of canopy chemicals in humid tropical forests. Remote Sensing of Environment 115:3587–3598.

Asner, G. P., P. G. Brodrick, C. B. Anderson, N. Vaughn, D. E. Knapp, and R. E. Martin. 2016. Progressive forest canopy water loss during the 2012–2015 California drought. Proceedings of the National Academy of Sciences USA 113:E249–E255.

Aubinet, M., T. Vesala, and D. Papale, editors. 2011. Pages 263–289Eddy covariance: a practical guide to measurement and data analysis. Spring Atmospheric Sciences, Berlin, Germany.

Baldocchi, D., C. Sturtevant, and C. Fluxnet. 2015. Does day and night sampling reduce spurious correlation between canopy photosynthesis and ecosystem respiration? Agricultural and Forest Meteorology 207:117–126.

Carlson, T. N., and D. A. Ripley. 1997. On the relation between NDVI, fractional vegetation cover, and leaf area index. Remote Sensing of Environment 62:241–252.

Carrascal, L. M., I. Galván, and O. Gordo. 2009. Partial least squares regression as an alternative to current regression methods used in ecology. Oikos 118:681–690.

Ciais, P., et al. 2005. Europe-wide reduction in primary productivity caused by the heat and drought in 2003. Nature 437:529–533.

Cook, B. D., et al. 2004. Carbon exchange and venting anomalies in an upland deciduous forest in northern Wisconsin, USA. Agricultural and Forest Meteorology 126:271–295.

Curran, P. J. 1989. Remote sensing of foliar chemistry. Remote Sensing of the Environment 30:271–278.

Desai, A. R., P. V. Bolstad, B. D. Cook, K. J. Davis, and E. V. Carey. 2005. Comparing net ecosystem exchange of carbon dioxide between an old-growth and mature forest in the upper Midwest, USA. Agricultural and Forest Meteorology 128:33–55.

Desai, A. R., et al. 2008. Cross site evaluation of eddy covariance GPP and RE decomposition techniques. Agricultural and Forest Meteorology 148(6–7):821–838.

Elvidge, C. D. 1990. Visible and near-infrared reflectance characteristics of dry plant materials. International Journal of Remote Sensing 11:1775–1795.

Falge, E., et al. 2001. Gap filling strategies for defensible annual sums of net ecosystem exchange. Agricultural and Forest Meteorology 107:43–69.

Feilhauer, H., G. P. Asner, R. E. Martin, and S. Schmidtlein. 2010. Brightness-normalized partial least squares regression for hyperspectral data. Journal of Quantitative Spectroscopy & Radiative Transfer 111:1947–1957.

Gamon, J. A. 2015. Reviews and syntheses: optical sampling of the flux tower footprint. Biogeosciences 12:4509–4523.

Gamon, J. A., J. Penuelas, and C. B. Field. 1992. A narrow-waveband spectral index that tracks diurnal changes in photosynthetic efficiency. Remote Sensing of Environment 41(1):35–44.

Gamon, J. A., L. Serrano, and J. S. Surfus. 1997. The photochemical reflectance index: an optical indicator of photosynthetic radiation use efficiency across species, functional types, and nutrient levels. Oecologia 112:492–501.

Garbulsky, M. F., J. Peñuelas, J. Gamon, Y. Inoue, and I. Filella. 2011. The photochemical reflectance index (PRI) and the remote sensing of leaf, canopy and ecosystem radiation use efficiencies: a review and meta-analysis. Remote Sensing of Environment 115 (2):281–297.

Geladi, P., and B. R. Kowalski. 1986. Partial least-squares regression—a tutorial. Analytica Chimica Acta 185:1–17.

Gittelson, A. A., and M. Merzlyak. 1996. Signature analysis of leaf reflectance spectra: algorithm development for remote sensing of chlorophyll. Journal of Plant Physiology 148:494–500.

Goulden, M. L., G. C. Winston, A. M. S. McMillan, M. E. Litvak, E. L. Read, A. V. Rocha, and J. R. Elliot. 2006. An eddy covariance mesonet to measure the effect of forest age on land-atmosphere exchange. Global Change Biology 12:2146–2162.

Goulden, M. L., R. G. Anderson, R. C. Bales, A. E. Kelly, M. Meadows, and G. C. Winston. 2012. Evapotranspiration along an elevation gradient in California's Sierra Nevada. Journal of Geophysical Research—Biogeosciences 117:G03028.

Green, R. O., et al. 1998. Imaging spectroscopy and the Airborne Visible Infrared Imaging Spectrometer (AVIRIS). Remote Sensing of Environment 65:227–248.

Grossman, Y. L., S. L. Ustin, S. Jacquemoud, E. W. Sanderson, G. Schmuck, and J. Verdebout. 1996. Critique of stepwise multiple linear regression for the extraction of leaf biochemistry information from leaf reflectance data. Remote Sensing of Environment 56:182–193.

Heinsch, F. A., et al. 2006. Evaluation of remote sensing based terrestrial productivity from MODIS using regional tower eddy flux network observations. IEEE Transactions on Geoscience and Remote Sensing 44:1908–1925.

Hochberg, E. J., D. A. Roberts, P. E. Dennison, and G. C. Hulley. 2015. Special issue on the Hyperspectral Infrared Imager (HyspIRI): emerging science in terrestrial and aquatic ecology, radiation balance and hazards. Remote Sensing of Environment 167:1–5.

Hook, S. J., J. E. J. Myers, K. J. Thome, M. Fitzgerald, and A. B. Kahle. 2001. The MODIS/ASTER airborne simulator (MASTER)—a new instrument for earth science studies. Remote Sensing of Environment 76:93–102.

Inoue, Y., J. Penuelas, A. Miyata, and M. Mano. 2008. Normalized difference spectral indices for estimating photosynthetic efficiency and capacity at a canopy scale derived from hyperspectral and CO_2 flux measurements in rice. Remote Sensing of Environment 112:156–172.

Jetz, W., et al. 2016. Monitoring plant functional diversity from space. Nature Plants 2:16024.

Jung, M., et al. 2011. Global patterns of land-atmosphere fluxes of carbon dioxide, latent heat, and sensible heat derived from eddy covariance, satellite, and meteorological observations. Journal of Geophysical Research 116:G00J07.

Kelly, A. E., and M. L. Goulden. 2008. Rapid shifts in plant distribution with recent climate change. Proceedings of the National Academy of Sciences USA 105:11823–11826.

Kljun, N., P. Calanca, M. W. Rotach, and H. P. Schmid. 2015. A simple two-dimensional parameterisation for Flux Footprint Prediction (FFP). Geoscientific Model Development 8:3695–3713.

Kobayashi, H., D. D. Baldocchi, Y. Ryu, Q. Chen, S. Ma, J. L. Osuna, and S. L. Ustin. 2012. Modeling energy and carbon fluxes in a heterogeneous oak woodland: a three-dimensional approach. Agricultural and Forest Meteorology 152:83–100.

Land Processes Distributed Active Archive Center (LP DAAC) (2015) MODIS GPP (MOD17A2.005). NASA EOSDIS Land Processes DAAC, USGS Earth Resources Observation and Science (EROS) Center, Sioux Falls, South Dakota, USA. https://lpdaac.usgs.gov

Lee, C. M., M. L. Cable, S. J. Hook, R. O. Green, S. L. Ustin, D. J. Mandl, and E. M. Middleton. 2015. An introduction to the NASA Hyperspectral InfraRed Imager (HyspIRI) mission and preparatory activities. Remote Sensing of Environment 167:6–19.

Lucht, W., C. B. Schaaf, and A. H. Strahler. 2000. An algorithm for the retrieval of albedo from space using semiempirical BRDF models. IEEE Transactions on Geoscience and Remote Sensing 38:977–998.

Martin, M. E., and J. D. Aber. 1997. High spectral resolution remote sensing of forest canopy lignin, nitrogen, and ecosystem processes. Ecological Applications 7:431–443.

Martin, M. E., L. C. Plourde, S. V. Ollinger, M. L. Smith, and B. E. McNeil. 2008. A generalizable method for remote sensing of canopy nitrogen across a wide range of forest ecosystems. Remote Sensing of Environment 112:3511–3519.

Matthes, J. H., S. H. Knox, C. Sturtevant, O. Sonnentag, J. Verfaillie, and D. Baldocchi. 2015. Predicting landscape-scale CO_2 flux at a pasture and rice paddy with long-term hyperspectral canopy reflectance measurements. Biogeosciences 12:4577–4594.

Myneni, R. B., et al. 2002. Global products of vegetation leaf area and fraction absorbed PAR from year one of MODIS data. Remote Sensing Environment 83:214–231.

Ollinger, S. V. 2011. Sources of variability in canopy reflectance and the convergent properties of plants. New Phytologist 189:375–394.

Ollinger, S. V., and M. L. Smith. 2005. Net primary production and canopy nitrogen in a temperate forest landscape: an analysis using imaging spectroscopy, modeling and field data. Ecosystems 8:760–778.

Penuelas, J., I. Filella, and J. A. Gamon. 1995. Assessment of photosynthetic radiation-use efficiency with spectral reflectance. New Phytologist 131(3):291–296.

Roberts, D. A., K. L. Roth, and R. L. Perroy. 2011. Hyperspectral vegetation indices. Pages 309–327 *in* P. S. Thenkabail, J. G. Lyon,

and A. Huete, editors. Hyperspectral remote sensing of vegetation. CRC Press, Boca Raton, Florida, USA.

Roujean, J. L., M. Leroy, and P. Y. Deschamps. 1992. A bidirectional reflectance model of the Earth surface for the correction of remote-sensing data. Journal of Geophysical Research—Atmospheres 97:20455–20468.

Running, S. W., R. R. Nemani, F. A. Heinsch, M. Zhao, M. Reeves, and H. Hashimoto. 2004. A continuous satellite-derived measure of global terrestrial primary production. BioScience 54:547–560.

Ryu, Y., D. D. Baldocchi, J. Verfaillie, S. Ma, M. Falk, I. Ruiz-Mercado, T. Hehn, and O. Sonnentag. 2010. Testing the performance of a novel spectral reflectance sensor, built with light emitting diodes (LEDs), to monitor ecosystem metabolism, structure and function. Agricultural and Forest Meteorology 150:1597–1606.

Schimel, D., R. Pavlick, J. B. Fisher, G. P. Asner, S. Saatchi, P. Townsend, C. Miller, C. Frankenberg, K. Hibbard, and P. Cox. 2015. Observing terrestrial ecosystems and the carbon cycle from space. Global Change Biology 21:1762–1776.

Serbin, S. P., D. N. Dillaway, E. L. Kruger, and P. A. Townsend. 2012. Leaf optical properties reflect variation in photosynthetic metabolism and its sensitivity to temperature. Journal of Experimental Botany 63:489–502.

Serbin, S. P., A. Singh, A. R. Desai, S. G. DuBois, A. D. Jablonsld, C. C. Kingdon, E. L. Kruger, and P. A. Townsend. 2015. Remotely estimating photosynthetic capacity, and its response to temperature, in vegetation canopies using imaging spectroscopy. Remote Sensing of Environment 167:78–87.

Sims, D. A., et al. 2008. A new model of gross primary productivity for North American ecosystems based solely on the enhanced vegetation index and land surface temperature from MODIS. Remote Sensing of Environment 112:1633–1646.

Singh, A., S. P. Serbin, B. E. McNeil, C. C. Kingdon, and P. A. Townsend. 2015. Imaging spectroscopy algorithms for mapping canopy foliar chemical and morphological traits and their uncertainties. Ecological Applications 25:2180–2197.

Smith, M.-L., S. V. Ollinger, M. E. Martin, J. D. Aber, R. A. Hallett, and C. L. Goodale. 2002. Direct estimation of aboveground forest productivity through hyperspectral remote sensing of canopy nitrogen. Ecological Applications 12:1286–1302.

Soenen, S. A., D. R. Peddle, and C. A. Coburn. 2005. SCS+C: a modified sun-canopy-sensor topographic correction in forested terrain. IEEE Transactions on Geoscience and Remote Sensing 43:2148–2159.

Thompson, D. R., B. C. Gao, R. O. Green, D. A. Roberts, P. E. Dennison, and S. R. Lundeen. 2015. Atmospheric correction for global mapping spectroscopy: ATREM advances for the HyspIRI preparatory campaign. Remote Sensing of Environment 167:64–77.

Townsend, P. A., J. R. Foster, R. A. Chastain, and W. S. Currie. 2003. Application of imaging spectroscopy to mapping canopy nitrogen in the forests of the central Appalachian Mountains using Hyperion and AVIRIS. IEEE Transactions on Geoscience and Remote Sensing 41:1347–1354.

Tucker, C. J. 1979. Red and photographic infrared linear combinations for monitoring vegetation. Remote Sensing of Environment 8(2):127–150.

Ustin, S. L., and J. A. Gamon. 2010. Remote sensing of plant functional types. New Phytologist 186:795–816.

Ustin, S. L., A. A. Gitelson, S. Jacquemoud, M. Schaepman, G. P. Asner, J. A. Gamon, and P. Zarco-Tejada. 2009. Retrieval of foliar information about plant pigment systems from high resolution spectroscopy. Remote Sensing of Environment 113:S67–S77.

Vane, G., R. O. Green, T. G. Chrien, H. T. Enmark, E. G. Hansen, and W. M. Porter. 1993. The airborne visible infrared imaging spectrometer (AVIRIS). Remote Sensing of Environment 44:127–143.

Vogelmann, J. E., B. N. Rock, and D. M. Moss. 1993. Red edge spectral measurements from sugar maple leaves. International Journal of Remote Sensing 14:1563–1575.

Wold, S., M. Sjöström, and L. Eriksson. 2001. PLS-regression: a basic tool of chemometrics. Chemometrics and Intelligent Laboratory Systems 58:109–130.

Wolter, P. T., P. A. Townsend, B. R. Sturtevant, and C. C. Kingdon. 2008. Remote sensing of the distribution and abundance of host species for spruce budworm in Northern Minnesota and Ontario. Remote Sensing of Environment 112:3971–3982.

Xu, K., S. Metzger, and A. R. Desai. 2017. Upscaling tower-observed turbulent exchange at fine spatio- temporal resolution using environmental response functions. Agricultural and Forest Meteorology 232:10–22.

Zarco-Tejada, P. J., J. R. Miller, T. L. Noland, G. H. Mohammed, and P. H. Sampson. 2001. Scaling-up and model inversion methods with narrowband optical indices for chlorophyll content estimation in closed forest canopies with hyperspectral data. IEEE Transactions on Geoscience and Remote Sensing 39:1491–1507.

Supporting Information

Additional supporting information may be found online at: http://onlinelibrary.wiley.com/doi/10.1002/eap.1733/full

Data Availability

Data available from the following. PLSR model code and results: https://doi.org/10.6084/m9.figshare.6020153.

Spectroscopy data: https://ecosis.org/#result/fac4e3cb-7ebb-42d9-a7e3-1273114d4efa.

NASA AVIRIS: https://aviris.jpl.nasa.gov/alt_locator/ and directly downloaded at ftp://popo.jpl.nasa.gov/2013_HyspIRI_Prep_Data/L2-Ortho_Reflectance/ and ftp://popo.jpl.nasa.gov/2014_HyspIRI_Prep_Data/L2-Ortho_Reflectance/.

Ameriflux tower data sites are listed in Appendix S1: Table S1.